







## Probing Chemical Enrichment in Extremely Metal-Poor Galaxies and First Galaxies

KEITA FUKUSHIMA <sup>1</sup>, KENTARO NAGAMINE <sup>1,2,3</sup>, AKINORI MATSUMOTO,<sup>4,5</sup> YUKI ISOBE <sup>4,5</sup>, MASAMI OUCHI <sup>6,4,7</sup>,  
TAKAYUKI R. SAITOH <sup>8</sup> AND YUTAKA HIRAI <sup>9,10</sup>

<sup>1</sup>Theoretical Astrophysics, Department of Earth and Space Science, Graduate School of Science, Osaka University, Toyonaka, Osaka 560-0043, Japan

<sup>2</sup>Kavli IPMU (WPI), The University of Tokyo, 5-1-5 Kashiwanoha, Kashiwa, Chiba, 277-8583, Japan

<sup>3</sup>Department of Physics & Astronomy, University of Nevada, Las Vegas, 4505 S. Maryland Pkwy, Las Vegas, NV 89154-4002, USA

<sup>4</sup>Institute for Cosmic Ray Research, The University of Tokyo, 5-1-5 Kashiwanoha, Kashiwa, Chiba 277-8582, Japan

<sup>5</sup>Department of Physics, Graduate School of Science, The University of Tokyo, 7-3-1 Hongo, Bunkyo, Tokyo 113-0033, Japan

<sup>6</sup>National Astronomical Observatory of Japan, National Institutes of Natural Sciences, 2-21-1 Osawa, Mitaka, Tokyo 181-8588, Japan

<sup>7</sup>Kavli Institute for the Physics and Mathematics of the Universe (WPI), University of Tokyo, Kashiwa, Chiba 277-8583, Japan

<sup>8</sup>Department of Planetology, Graduate School of Science, Kobe University, 1-1 Rokkodai-cho, Nada-ku, Kobe, Hyogo 657-8501, Japan

<sup>9</sup>Department of Physics and Astronomy, University of Notre Dame, 225 Nieuwland Science Hall, Notre Dame, IN 46556, USA

<sup>10</sup>Astronomical Institute, Tohoku University, 6-3 Aoba, Aramaki, Aoba-ku, Sendai, Miyagi 980-8578, Japan

### ABSTRACT

The chemical composition of galaxies offers vital insights into their formation and evolution. A key aspect of this study is the correlation between helium abundance (He/H) and metallicity, which is instrumental in estimating the primordial helium generated by Big Bang nucleosynthesis. We study the chemical enrichment history of low-metallicity galaxies, specifically focusing on extremely metal-poor galaxies (EMPGs) and the first galaxies, using the one-zone model and cosmological hydrodynamic simulations. Our one-zone model, using the [Limongi & Chieffi \(2018\)](#) yield, aligns well with observed high He/H ratios at low metallicities and reproduces Fe/O ratios akin to EMPGs. Conversely, the [Nomoto et al. \(2013\)](#) yield does not fully match the high Fe/O ratios seen in EMPGs. Our cosmological hydrodynamic simulations of the first galaxy successfully replicate the stellar mass and star formation rate (SFR) of galaxies like GN-z11 but fail to produce metallicity and high He/H at low O/H. This is consistent with the results of the one-zone model, which shows that the slope of the He/H–O/H relation is moderate in young, actively star-forming galaxies, suggesting the importance of using galaxies with similar star formation histories for the fit. These results highlight the need for high-resolution simulations and expanded observational datasets to refine our understanding of early galactic chemical evolution.

**Keywords:** galaxies: abundances — galaxies: dwarf — galaxies: high-redshift — galaxies: evolution — methods: numerical

### 1. INTRODUCTION

Galaxy evolution begins with the first galaxies, which also mark the initial sites of metal enrichment in the universe. Advanced cosmological hydrodynamic simulations indicate that these primordial galaxies, existing at redshifts greater than 10 ( $z > 10$ ), are characterized by notably low metallicities ( $Z = 0.01 - 0.001 Z_{\odot}$ ) and relatively low stellar masses ( $M_{\star} \lesssim 10^6 M_{\odot}$ ) ([Wise et al. 2012](#); [Johnson et al. 2013](#); [Kimm & Cen 2014](#); [Romano-Díaz et al. 2014](#); [Yajima et al. 2017, 2023](#)).

The James Webb Space Telescope (JWST) has discovered galaxies at  $z > 10$  with spectroscopic confirma-

tion of redshifts ([Roberts-Borsani et al. 2023](#); [Williams et al. 2023](#); [Curtis-Lake et al. 2023](#); [Bunker et al. 2023](#); [Arrabal Haro et al. 2023a,b](#); [Harikane et al. 2024, 2023](#)), which also allow the investigation of mass–metallicity relation (MZR) for high- $z$  galaxies ([Curti et al. 2023a](#); [Nakajima et al. 2023](#)). In particular, GN-z11, noted for its significant mass at high redshifts, has garnered considerable attention and been the focus of numerous detailed observational studies ([Cameron et al. 2023](#); [Bunker et al. 2023](#); [Senchyna et al. 2023](#); [Isobe et al. 2023](#)).

However, observing low-mass galaxies in the early universe is still difficult without the aid of the gravitational

lensing effect. [Isobe et al. \(2022\)](#) found that  $\text{H}\alpha$  emission of galaxies with stellar masses of  $M_\star \sim 10^6 M_\odot$  is only detected at  $z < 1$  with JWST and up to  $z < 2$  with forthcoming Thirty Meter Telescope (TMT) without the gravitational lensing effect (c.f. [Vanzella et al. 2023](#)).

The Extremely Metal-Poor Galaxies (EMPGs) could be the local analog of low-mass first galaxies, and might help to understand the properties of first galaxies. EMPGs have low stellar masses ( $M_\star < 10^7 M_\odot$ ), low metallicities ( $Z < 0.1 Z_\odot$ ), and high specific star formation rates ( $\text{sSFR} \sim 100 \text{ Gyr}^{-1}$ ), which are similar to the characteristics of the first galaxies ([Kojima et al. 2020](#)). [Curti et al. \(2023b\)](#) examined the MZR for low-mass galaxies at  $3 < z < 10$  observed using gravitational lensing effects and found it to be comparable to the MZR of nearby ‘Blueberry’ galaxies ([Yang et al. 2017](#)). Studying EMPGs provides a unique opportunity to decipher the formation history of the first galaxies.

The chemical evolution of EMPGs is poorly understood. High Fe/O close to the solar abundance has been observed for some EMPGs ([Izotov et al. 2018a](#); [Kojima et al. 2021](#)). Chemical evolution model calculations ([Isobe et al. 2022](#); [Watanabe et al. 2023](#)) suggest the need for brighter hypernovae and/or pair-instability supernovae (PISNe), which are caused by massive stars ([Barkat et al. 1967](#); [Heger & Woosley 2002](#); [Umeda & Nomoto 2002](#); [Nomoto et al. 2013](#)). This distinction is crucial because young galaxies in the low-metallicity regime are often characterized by a top-heavy initial mass function (IMF). However, these model calculations do not consider realistic star formation histories and gas dynamics, and need to be validated using cosmological hydrodynamic simulations.

Hydrodynamic simulations have been used to study the star formation and chemical evolution of local dwarf galaxies ([Wetzel et al. 2016](#); [Hirai et al. 2017](#); [Revaz & Jablonka 2018](#); [Wheeler et al. 2019](#); [Agertz et al. 2020](#); [Gutcke et al. 2022](#)). For example, the Latte project performed a high-resolution simulation of the Milky Way-type galaxy using the GIZMO code ([Hopkins 2015](#)) with the FIRE-2 model ([Hopkins et al. 2018](#)), and studied the surrounding dwarf galaxies with  $M_\star > 10^5 M_\odot$ . The mass–metallicity relation (MZR) is consistent with observations, and these low-mass galaxies quenched 3–11 Gyr ago from today ([Wetzel et al. 2016](#)). Their simulated dwarf galaxies with  $M_\star < 10^5 M_\odot$  have lower metallicities in the stellar MZR than the observed data, which could be due to the metal contamination by Population III (Pop III) and PISNe, as well as the environmental effects ([Wheeler et al. 2019](#)). Star formation in low-mass galaxies with  $M_\star < 10^5 M_\odot$  is suppressed by reionization, while those with  $M_\star > 10^5 M_\odot$  are mainly

quenched by gas stripping and supernova (SN) feedback ([Rodríguez Wimberly et al. 2019](#)). Therefore, galaxies in this mass range are also a good test of SN feedback models.

Additionally, the impact of reionization on low-mass galaxy evolution is significant. As demonstrated in previous studies, when gas in these galaxies is heated above the virial temperature due to reionization, star formation ceases ([Wetzel et al. 2016](#); [Rodríguez Wimberly et al. 2019](#)). Subsequently, as the halo mass grows and the virial temperature rises, star formation may resume. Therefore, the details of the reionization process are important for the evolution of dwarf galaxies ([Benítez-Llambay & Frenk 2020](#)).

The abundance ratio He/H can be examined as a function of metallicity to estimate the primordial He abundance, but this relation is highly uncertain ([Matsumoto et al. 2022](#)). [Vincenzo et al. \(2019\)](#) show the relation between He/H and  $12+\text{O}/\text{H}$  using a one-zone model and cosmological chemodynamical simulation. They compared [Nomoto et al. \(2013\)](#) and [Limongi & Chieffi \(2018\)](#) yield models for core-collapse supernovae (CCSNe), and [Karakas \(2010\)](#) and [Ventura et al. \(2013\)](#) for asymptotic giant branch (AGB) yields. This showed that He/H was particularly high when using the [Limongi & Chieffi \(2018\)](#) yield, which considers the effect of the WofR–Rayet star at the low-metallicity range.

In this study, we aim to elucidate specific aspects of the formation and evolution of EMPGs. To do this, we use both the one-zone model and cosmological hydrodynamic simulations focusing on the first galaxy. The one-zone model was performed to understand the fundamental parameters that affect the evolution of galaxies with low metal abundances and young ages, such as EMPG galaxies and first galaxies, and the extent to which different yields alter chemical evolution. The simulations of the first galaxies are performed to solve the chemical evolution of young galaxies with realistic baryon cycles that cannot be handled by the one-zone model.

This paper is organized as follows. Section 2 details our methodology, outlining the one-zone model and the cosmological hydrodynamic simulation. Section 3.1 focuses on assessing the effects of metallicity on He/H and Fe/O ratios in a one-zone model, considering two different yield models. Section 3.2 explores the impact of the baryon cycle on chemical evolution in the first galaxy using cosmological hydrodynamic simulations. In Section 4.1, we discuss the impact of yield differences on He enrichment in the first galaxies, and in Section 4.2 we discuss how primordial He abundance should be obtained using the observed galaxies. We then conclude in Section 5.

## 2. METHOD

### 2.1. One-zone Box Model

We follow the calculation of the one-zone box model by Kobayashi & Taylor (2023); Kobayashi & Ferrara (2023), see Appendix A for details. Here, we calculate the outflow rate depending on the energy injection from the stars, and the energy release rate calculated by CELIB code (Saitoh 2016, 2017), which is coupled to our star formation and feedback model (Shimizu et al. 2019). We run 400 model calculations, each focusing on different parameters to explore a range of scenarios. The varied parameters include the star formation timescale  $t_s$ , gas inflow timescale  $t_i$ , gas outflow rate  $f_o$ , and the fraction of metals in the inflowing gas  $f_{inf}$ . To provide a clear and organized overview of these models and their parameters, we have summarized the details in Table 1.

Chemical evolution is computed using the CELIB code (Saitoh 2016, 2017), which incorporates the effects of CCSNe, type Ia supernovae (SN Ia), and AGB stars. The CCSNe yield of Nomoto et al. (2013), the SN Ia yields of Seitenzahl et al. (2013), the AGB star yields of Karakas (2010) and the super AGB star yields of Doherty et al. (2014) were used. The Chabrier (2003) IMF is adopted with a stellar mass range of 0.1–100  $M_\odot$ . We also conducted an additional calculation using the Limongi & Chieffi (2018) yields for CCSN as an alternative to the Nomoto et al. (2013) yields, facilitating a comparative analysis. When calculating the yield of Limongi & Chieffi (2018), we took into account an empirical law of the star’s rotational velocity for each metallicity of the star.

We treat stars with  $Z \leq 10^{-5} Z_\odot$  as Pop III, and adopt the following yield tables for the Pop III stars: the CCSNe yield of Nomoto et al. (2013), the AGB star yields of Campbell & Lattanzio (2008) and Gil-Pons et al. (2013), and the top-heavy IMF from Susa et al. (2014). In the CCSNe yield of Pop III, we also include the contribution from PISN (Nomoto et al. 2013). A delay-time distribution function with a power law of  $t^{-1}$  was used for the SN Ia event rate (Totani et al. 2008; Maoz & Mannucci 2012; Maoz et al. 2014), which is turned on after  $4 \times 10^7$  yr. The hypernovae blending fraction  $f_{HN}$  is set to 0.05. The details of the above yield tables are given in Fukushima et al. (2023).

### 2.2. Cosmological Zoom-in Hydrodynamic Simulations

We use the cosmological N-body/smoothed particle hydrodynamics (SPH) code GADGET3-OSAKA (Shimizu et al. 2019; Nagamine et al. 2021). This code includes star formation, SN feedback, ultraviolet background (UVB) radiation, and metal cooling, which are implemented in the updated version of GADGET-3,

**Table 1.** Summary of our one zone model parameters. See Appendix A for the definition of the parameters.

$t_{sf}$ (yrs)	$t_{in}$ (yrs)	$f_o$	$f_{inf}$
$10^6$	$10^7$	0.0	0.0
$10^7$	$10^8$	0.01	0.01
$10^8$	$10^9$	0.1	0.1
$10^9$	$10^{10}$	1.0	1.0
$10^{10}$	–	10	–

initially based on GADGET-2 (Springel 2005). We adopt the following standard  $\Lambda$  cosmological parameters from Planck Collaboration et al. (2016):  $\Omega_m = 0.3089$ ,  $\Omega_{DM} = 0.2603$ ,  $\Omega_b = 0.04864$ ,  $\sigma_8 = 0.8150$ , and  $h = 0.6776$ .

Calculations for photoheating and photoionization under the influence of UVB and radiative cooling are implemented using the Grackle-3 chemistry and cooling library (Smith et al. 2017). It handles primordial chemical reactions involving atomic H, D, He, and the molecules  $H_2$  and HD (with `primordial_chemistry` = 3, comprising 12 species). In addition, it incorporates photoheating and photoionization from the UV background. In our simulations, we use the uniform UVB model by Haardt & Madau (2012), which is activated from  $z = 15$ . We employ the Osaka SN feedback model (Shimizu et al. 2019), which includes thermal and kinetic feedback mechanisms. The nucleosynthetic yield is compiled using the CELIB, the same as in Sec 2.1.

We performed simulations for the first galaxy using a zoom-in box size of  $(2.5 h^{-1} \text{cMpc})^3$  within the outer full box of  $(100 h^{-1} \text{cMpc})^3$ . The dark matter particle mass is  $1.6 \times 10^4 h^{-1} M_\odot$ , the SPH particle mass is  $3.2 \times 10^3 h^{-1} M_\odot$ , and the gravitational softening length is  $200 h^{-1}$  cpc. It was conducted up to  $z = 10$ , with the largest halo mass in our simulation box at this redshift exceeding  $7 \times 10^{10} h^{-1} M_\odot$ , and the final stellar mass around  $3 \times 10^9 h^{-1} M_\odot$ .

We also simulated two first galaxies with mass resolution is 8 times worse that varied the CCSNe yield to discuss the effect from different yields (Nomoto et al. (2013) and Limongi & Chieffi (2018)) in our model at Sec. 4.1.

We used the MUSIC code (Hahn & Abel 2011) to produce the initial conditions at  $z = 99$ .

## 3. RESULT

### 3.1. One zone model

We start by presenting the chemical abundance from our one-zone model calculations in Figure 1. The first set of panels (*a* and *c*) employs the Nomoto et al. (2013)

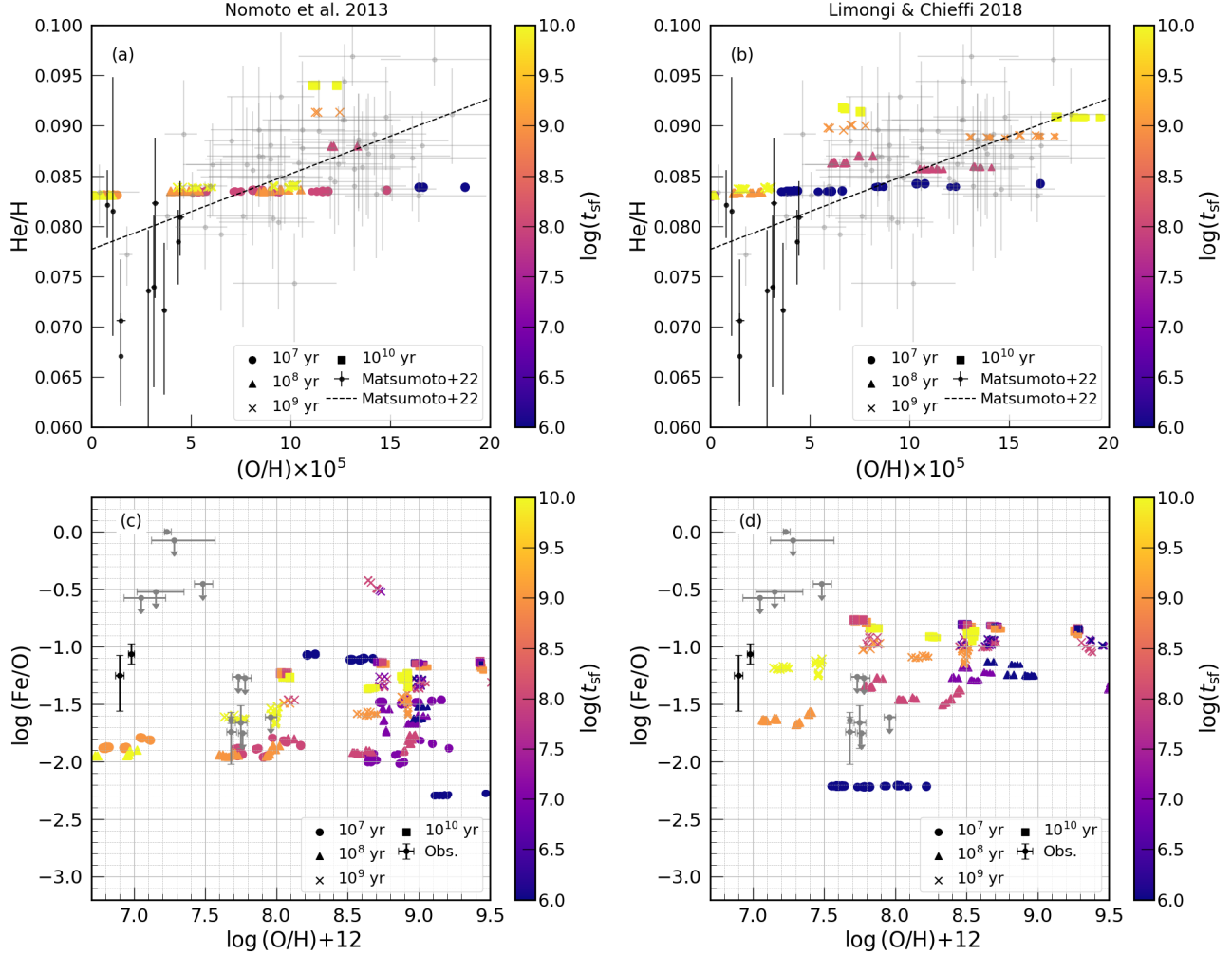


**Figure 1.** *Panel (a):* Evolution of He/H with metallicity from our one-zone model calculations. The different symbols indicate the chemical abundance of the galaxies at different ages in our model calculations. The color bar indicates  $t_{\text{sf}}$ . Black and gray points are the results of Matsumoto et al. (2022) and Hsyu et al. (2020), respectively. The black dashed line is the best linear fit of the observational data points obtained by Matsumoto et al. (2022). *Panel (b):* The same figure as panel (a) is plotted using the yields of Limongi & Chieffi (2018). *Panel (c):* The evolution of Fe/O with metallicity. Data points with black and gray error bars show the observed galaxies’ chemical abundance (Izotov et al. 2018b; Kojima et al. 2020, 2021; Isobe et al. 2022). Galaxies with high Fe/O at low metallicity, particularly interesting for this study, are shown in black solid points. *Panel (d):* The same figure as panel (b) is plotted using the yields of Limongi & Chieffi (2018).

yield to explore He/H and Fe/O ratios in relation to metallicity, respectively, while the second set (b and d) utilizes the Limongi & Chieffi (2018) yield for a similar calculation. The circle, triangle, cross, and square symbols in the scatter plot indicate the different ages  $10^6$ ,  $10^7$ ,  $10^8$ ,  $10^9$ , and  $10^{10}$  yr of the one-zone galaxy since the beginning of star formation, respectively. The colors indicate the star formation timescale ( $t_{\text{sf}}$ ), which are defined in the Appendix A. In the models characterized by a short  $t_{\text{sf}}$  or a high  $f_o$ , the calculation halts once their gas reservoirs are depleted. As a result, for certain samples, data points at the  $10^9$ – $10^{10}$  year mark are

not represented. In panels (a) and (b), the black dots are the observations of EMPGs (Matsumoto et al. 2022), and the gray dots are the observations of dwarf galaxies (Hsyu et al. 2020). The black dashed line is the linear fit, performed by Matsumoto et al. (2022). In panel (c) and (d), black dots (high Fe / O and low O / H) and gray dots are the observed values (Izotov et al. 2018b; Kojima et al. 2020, 2021; Isobe et al. 2022). The size of the symbol reflects the value of  $f_o$ .

In Panel (a), our one-zone model results show a discrepancy with certain EMPG observations; notably, none of our modeled points exhibit He/H ratios lower

than 0.082. This deviation primarily stems from our model's adoption of a higher primordial He abundance, as suggested by Planck Collaboration et al. (2016), compared to the baseline (O/H)=0 He/H ratio determined by Matsumoto et al. (2022). Additionally, the slope of our modeled He/H versus O/H relationship is shallower than the observed fitting line. This suggests that in our model, He enrichment from CCSNe and AGB stars has a limited impact on altering the He/H abundance ratio, largely due to the predominance of primordial gas in the galaxy's composition as per our setup. However, it is important to consider the substantial error margins and variability in the observed data. Notably, high He/H ratios ( $> 0.085$ ) are achievable in galaxies approximately 1–10 Gyr old, characterized by large  $f_o$ , low  $t_{sf}/t_{in}$  ratios, and low gas fractions at 1–10 Gyr. Consequently, the chemical composition of these galaxies is likely influenced more significantly by the local effects of nearby AGB stars.

In panel (b), similar to panel (a), we see that the He/H ratio does not fall below 0.082. For values of  $(O/H) \times 10^5 \gtrsim 10$ , our model achieves He/H ratios that are comparable to, or marginally lower than, the fitting line of the observation established by Matsumoto et al. (2022). This outcome can be attributed to the yields from Limongi & Chieffi (2018), which result in significantly less hydrogen ejection compared to those from Nomoto et al. (2013). Although this yield model does not fully replicate the high He/H observations at low metal abundances noted by Hsyu et al. (2020), it exhibits a wider dispersion than the results using the Nomoto et al. (2013) yield, as shown in panel (a). The  $10^8$ -year-old galaxies with  $O/H=7.5$ –10 and  $He/H=0.087$  follow the same evolution as the high He/H galaxies in panel (a).

Galaxies with chemical abundance comparable to the fitting line from the observations (Matsumoto et al. 2022) have roughly the same He/H and different O/H at each age, and their  $t_{sf}$  are comparable. This is due to the fact that the data sets have different  $f_o$  and  $f_{inf}$ , but the same  $t_{in}$ . After checking these samples, we found that the slope of the He/H-O/H relationship seems to be larger for galaxies with larger  $t_{sf}$  and  $t_{in}$ .

In panel (c), our model illustrates that galaxies with a  $\log(O/H) \sim 7.0$  have a lower Fe/O ratio compared to what is observed. This difference is primarily attributed to the central role of CCSNe in the chemical evolution of these young galaxies in our model. Initially, a high Fe/O ratio is observed due to metal enrichment by Pop III stars (as detailed in Appendix B), but this ratio is rapidly diminished by the enrichment of alpha elements from conventional CCSNe. Addition-

ally, our results indicate that galaxies around 1 Gyr old can exhibit relatively high Fe/O ratios (around  $-0.5$ ). Although EMPGs also display high Fe/O ratios, they possess a greater gas fraction compared to those of the modeled galaxies. This divergence is likely due to more pronounced iron enrichment from SNIa in our galaxy sample, which is facilitated by their lower gas fractions.

Panel (d), in contrast to panel (c), shows a galaxy with an age of  $10^9$  yr with  $\log(Fe/O) \sim -1.2$  and  $\log(O/H) < 7.5$ , this chemical abundance close to the observed galaxies.

In summary, the use of Nomoto et al. (2013) yields in our models successfully replicates observed galactic chemical properties for certain parameters. However, it falls short of accurately matching other aspects, such as the gas fraction, when compared to observations. In contrast, the application of Limongi & Chieffi (2018) yields appears to align more closely with observational data, offering a more consistent representation of the chemical evolution in galaxies.

### 3.2. Chemical enrichment in first galaxies

In this section, we analyze our simulation results for galaxies at  $z = 10$ . Our focus is on examining the chemical evolution of young galaxies, leveraging a more realistic baryon cycle in our cosmological hydrodynamic simulations, surpassing the limitations of the conventional one-zone model.

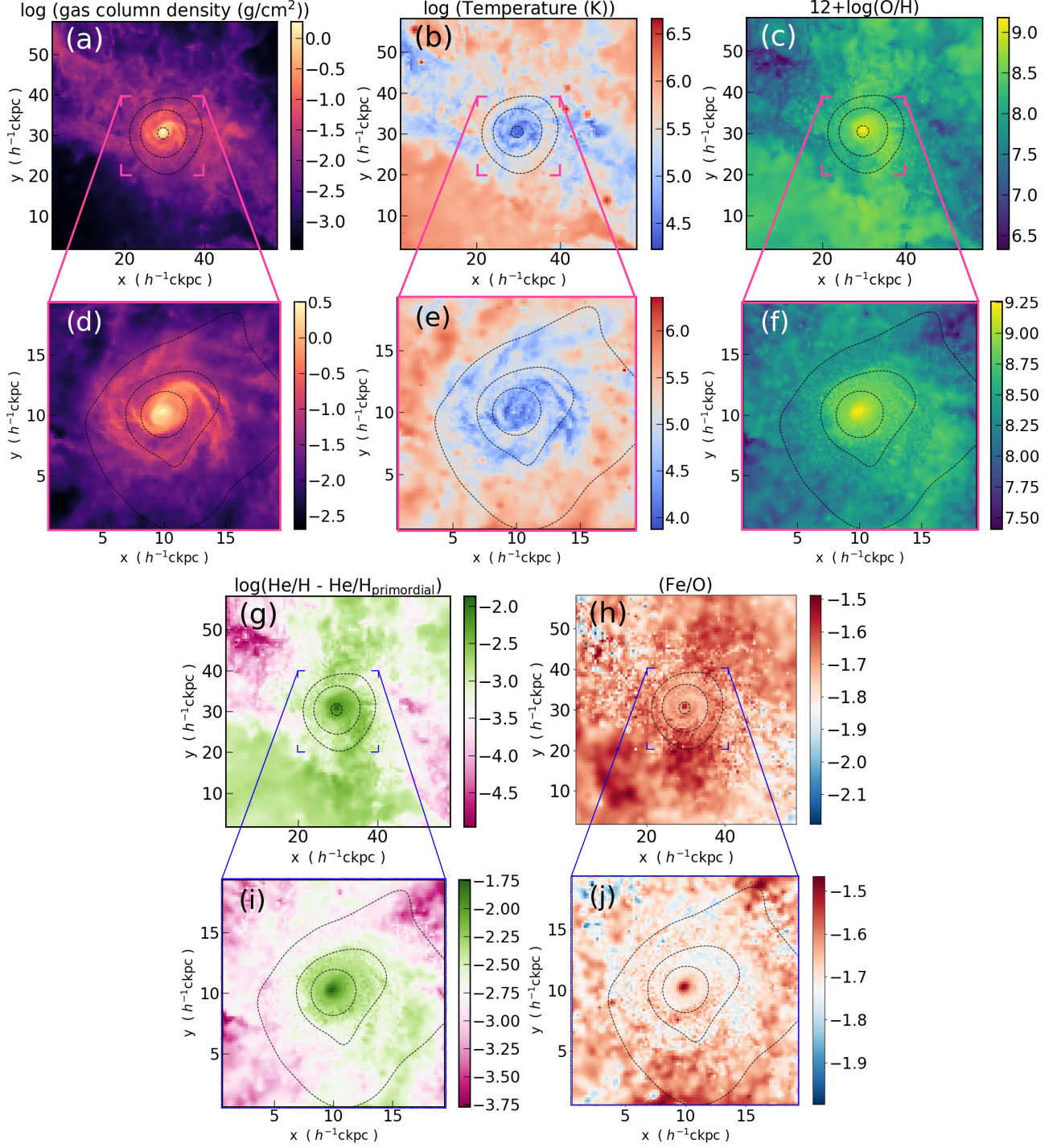
#### 3.2.1. Spatial distribution of gas and metals in first galaxies

Figure 2 shows the gas density (panels a, d), mass-weighted temperature (b, e), metallicity (c, f), gas phase He/H (g, i), and gas phase Fe/O (h, j) distribution in our first galaxy simulation. The top figures show a  $(60 h^{-1} \text{ckpc})^3$  region projected onto one plane, and the bottom figures for the central  $(20 h^{-1} \text{ckpc})^3$  region. The black-dotted contour shows the stellar surface density of  $\log(\Sigma_\star [\text{g}/\text{cm}^2]) = 0.0, -1.0, -2.0$ .

Panel (a) illustrates a galaxy in the process of formation, situated at the core of a larger filamentary structure. Panel (d) reveals that this galaxy has developed a well-defined disk, featuring spiral arms predominantly composed of colder gas, with temperatures below  $10^{4.5}$  K, as detailed in Panel (e).

Panel (b) displays the colder gas, with temperatures less than  $10^5$  K, within the filament, contrasted against the surrounding higher temperature gas, exceeding  $10^6$  K, enveloping the filament.

Panel (c) reveals that the filament is characterized by low metallicities, around  $\log(O/H) + 12 \simeq 6.5$ . In contrast, gas with higher metallicity is seen flowing out



**Figure 2.** Gas column density (panels *a*, *d*), mass-weighted temperature (*b*, *e*), metallicity (*c*, *f*), He/H (*g*, *i*), and Fe/O (*h*, *j*) distribution in our first galaxy simulation at  $z = 10$ . The upper panels for each property show the  $(60 h^{-1} \text{ckpc})^3$  region projected onto a plane, and the lower panels zoom in to the central  $(20 h^{-1} \text{ckpc})^3$  region. The black-dotted contours show the distribution of stars, each of which indicates the stellar surface density of  $\log(\Sigma_{\star}[\text{g/cm}^2]) = 0.0, -1.0, -2.0$ .

perpendicularly to the filament, a process attributed to SN feedback. Meanwhile, Panel (*f*) depicts varied metallicities within the galaxy: the central part exhibits high metallicity ( $\log(\text{O/H}) + 12 \gtrsim 9.1$ ), the

disk component with a stellar surface density between  $-1.0 < \log(\Sigma_{\star}[\text{g/cm}^2]) < 0.0$  shows a metallicity of  $\log(\text{O/H}) + 12 \sim 8.8$ , and the disk regions with densi-

ties from  $-2.0 < \log(\Sigma_\star [\text{g}/\text{cm}^2]) < -1.0$  have lower metallicity, approximately  $\log(\text{O}/\text{H}) + 12 \sim 8.4$ .

Panel (g) illustrates that the filament predominantly exhibits a primordial abundance and He-rich gas being expelled from the galaxy due to outflows, as indicated in panel (c). Meanwhile, Panel (i) highlights that the He-rich gas is more densely concentrated in the central regions of the galaxy.

Panel (h) reveals that the gas flowing into the filament primarily exhibits a high Fe/O, except in certain clumpy regions where Fe/O is lower. Panel (j) further shows these clumpy low Fe/O regions within the cooler, denser areas of the disk-like structure (as indicated in panels e and d). This pattern of distribution may be attributable to oxygen enrichment by CCSNe in star-forming regions.

### 3.2.2. Redshift evolution of physical quantities in first galaxies at $z > 10$

Figure 3 presents various properties of the first galaxy as functions of redshift: stellar mass (panel a), star formation rate (SFR) (panel b), metallicity (panel c), and Fe/O (panel d). For panels (c) and (d), the measurements reflect the metallicity and Fe/O of the gas phase within a region twice the radius of the galaxy's half-stellar mass. The black data points represent observed values for GN-z11 (Bunker et al. 2023).

Our simulation shows the galaxy attaining the observed stellar mass at the same redshift, and the SFR is also consistent with the observed value at  $z \sim 11$ . Notably, our model predicts a peak in star formation at  $z \sim 10$ . However, the gas-phase metallicity of the galaxy reaches solar levels by  $z = 12.2$ , which is about ten times higher than the observed values.

The Fe/O of the first galaxies is below the abundance ratios observed in EMPGs at  $z = 0$ , as depicted in Fig. 1(b). The increase in Fe/O at  $z < 12$  can be attributed to metal enrichment by CCSNe from low-mass progenitors with  $\sim 13 M_\odot$  and by SN Ia.

### 3.2.3. Distribution of He in first galaxies

Figure 4 shows the chemical abundance distribution of gas within a radius twice the half-stellar mass radius of our simulated first galaxy. The color indicates the gas mass in each bin of the plotted parameter space. The He/H and metallicity values depicted in Figs. 2(f) and 2(i) fall in between the two black lines. Essentially, this means that when projecting the distribution from individual particle data onto a 2D parameter space of He/H vs. metallicity, there's a noticeable reduction in scatter to a narrow region between the two black lines.

The helium abundance of the SPH particles in our first galaxy has a shallower slope than the observed one by Matsumoto et al. (2022). Although there is a small

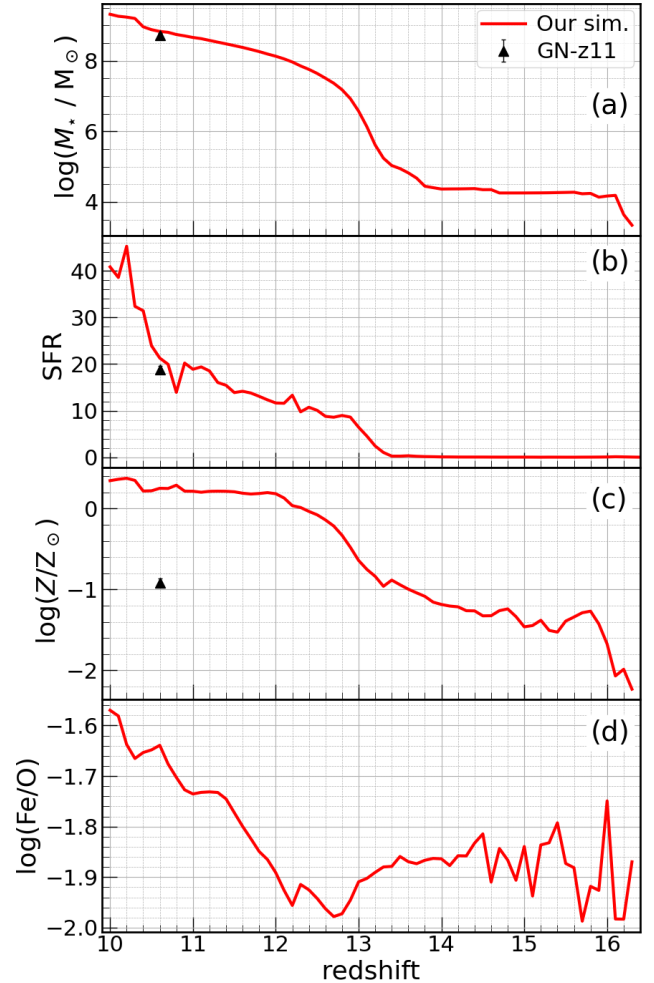


**Figure 3.** Evolution of the first galaxy in our cosmological hydrodynamic zoom-in simulation. Panels (a)–(d) show the redshift evolution of stellar mass, SFR ( $M_\odot/\text{yr}$ ), metallicity, and Fe/O, respectively. The black data points are the observed values of GN-z11 (Bunker et al. 2023).

amount of gas with high He/H ratios in the galaxy, it is insufficient to match the significant scatter of observed data points shown in Fig. 1a and reproduce the observed slope. The scatter in He abundance increases with increasing O/H.

At similar metallicities, low He/H ratios are typically due to CCSNe enrichment, while higher He/H ratios are attributed to AGB-star contributions. Therefore, both effects need to be considered. However, in regions of lower metallicity, the dispersion is smaller, suggesting a dominance of CCSNe elemental contamination.

The region between the two black lines exhibits limited dispersion, indicating that gas with low metallicity and high He/H ratio has a minimal impact on the projection effect.

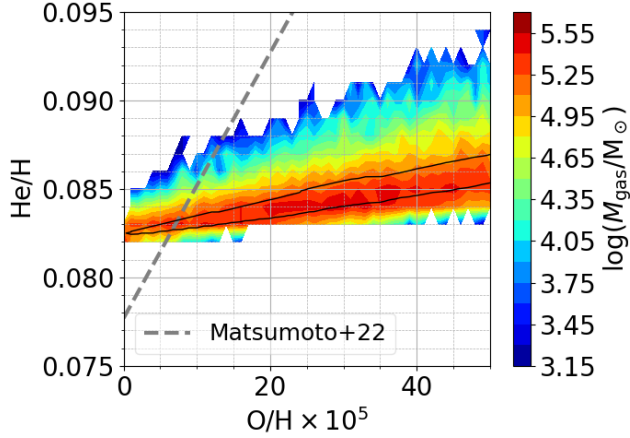


**Figure 4.** Gas phase He/H – O/H relation of the simulated galaxy at  $z = 10$ . The gas particles within twice the half-stellar mass radius were used to make the plot. The two solid black lines delineate the He/H–O/H relation as extracted from the two-dimensional distribution of He/H and metallicity shown in Figs. 2*i* and 2*f*.

Our result is consistent with previous work by Vincenzo et al. (2018) using a one-zone model and cosmological hydrodynamic simulation. Their result showed a small dispersion and a narrow slope in the He/H–metallicity relation at  $(\text{O}/\text{H} + 12) \lesssim 8.3$ .

Figures 1*a* and 4 demonstrate the challenge in accurately simulating the He/H in young, low-metallicity galaxies such as EMPGs and first galaxies when using the Nomoto et al. (2013) yields. We identify two key discrepancies in our findings: (i) the abundance distribution within individual galaxies fails to reproduce the observed slope and dispersion associated with a high gas fraction (Figs. 1*a*); (ii) contrary to observational data, our analysis does not reveal any gas with low O/H and high He/H ratios, even when examining spatially resolved gas in our first galaxy (Fig. 4). These inconsistencies suggest the necessity of a mechanism that can facilitate increased He release into the ISM, such as CCSNe yield proposed by Limongi & Chieffi (2018) as shown in Fig. 1*b*.

#### 4. DISCUSSION

##### 4.1. First galaxy simulations employing different yield models

In this section, we present a comparative analysis of simulations conducted using different yield models for the first galaxies, as detailed in Section 3.2. These simulations incorporate the yields from Nomoto et al. (2013) and Limongi & Chieffi (2018). Note that the mass resolution in these simulations is eight times lower than that

used in Section 3.2 to save computing time only for this comparison.

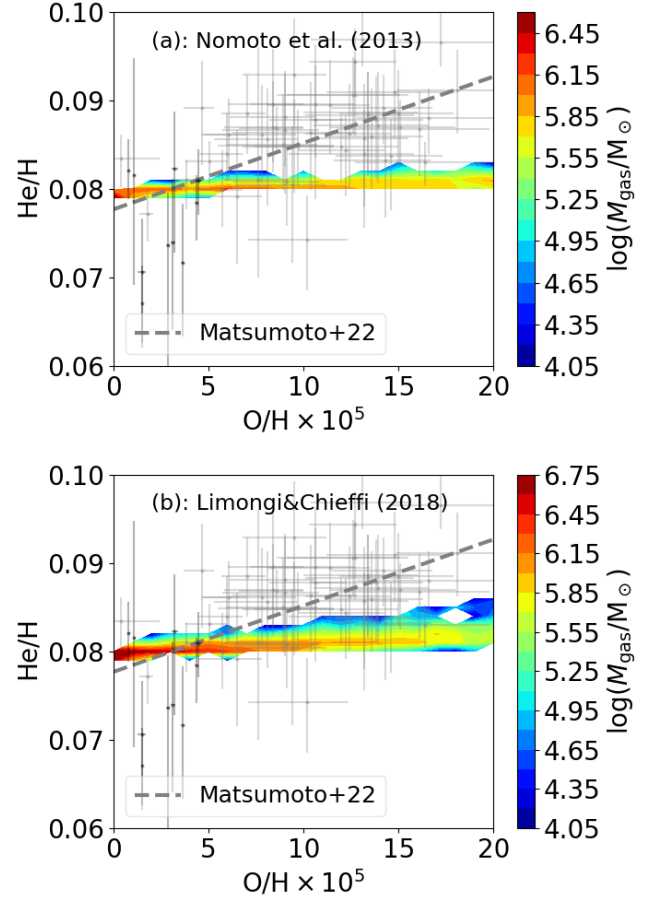


**Figure 5.** Comparison of gas phase He/H – O/H relation employing different yield models of (a) Nomoto et al. (2013) and (b) Limongi & Chieffi (2018) for the first galaxies at  $z = 11$ . Similar to Fig. 4, this analysis was performed using gas particles located within twice the half-stellar mass radius.

Figure 5 illustrates the O/H – He/H relationship, comparing the outcomes of simulations using different yield models of Nomoto et al. (2013) (panel *a*) and Limongi & Chieffi (2018) (panel *b*) at  $z = 10$ .

Panel (a) closely resembles Figure 4, yet it differs in several key aspects: the mass resolution is altered, the redshift is different, and it presents a broader range of both metallicity and He/H values. Interestingly, the variance observed here is even smaller than that in Figure 4. For instance, in the high-resolution scenario of Figure 4, the variation between the maximum and minimum He/H values at an O/H ratio of at  $\text{O}/\text{H} \times 10^5 = 20$  is  $\Delta\text{He}/\text{H} \sim 0.006$ , while for the low resolution case,  $\Delta\text{He}/\text{H} \sim 0.003$ . This reduced variance might be at-

tributable to the lower resolution, but further investigation is required to confirm this hypothesis.

In panel (b), we observe a slightly larger variance in the He/H ratio compared to panel (a). This increased variance can be attributed to the contamination of high He/H gas, resulting from lesser H enrichment by the yields of rotating stars, as depicted in Figure 1(b). However, this dispersion is smaller than that seen in Fig. 1(b).

In Fig. 1(b), we note that the He/H ratio is higher for higher stellar lifetimes  $t_{\text{sf}}$ , when other parameters are fixed. In our first galaxy simulations, star formation is active, suggesting that the effective  $t_{\text{sf}}$  in these scenarios would be relatively short. This characteristic of active star formation likely contributes to the more gradual slope observed in the simulated He/H – O/H relationship.

In our analysis, the role of PISNe in reproducing the high Fe/O ratios in EMPGs, as suggested by Watanabe et al. (2023), appears insufficient when considering the observed He/H–O/H relation depicted in our Fig. 1(a) and 4. Additionally, the introduction of WR stars in Watanabe et al. (2023)’s study to explain the N/O ratios observed in GN-z11 may also impact the He/H–O/H relation. However, the He/H–O/H relation is intricately tied to the star formation history of galaxies, underscoring the need for further investigation to fully comprehend these complex dynamics.

#### 4.2. How to Estimate the Primordial He/H Ratio

The insights drawn from Figures 1(a, b), 4, and 5 imply that accurately determining the primordial He/H ratio from observational data might necessitate focusing on galaxies with comparable SFR, and isolating the He/H ratio at a zero metallicity, a step that could be crucial for precise measurements.

Fig. 4 and 5 examine the gas phase He/H–O/H within the first galaxy. These figures demonstrate that replicating the steep slope observed in empirical data is not feasible. This finding suggests that the observed high He/H at low O/H levels are not merely the result of observing specific, atypical gas within galaxies. Furthermore, galaxies with active star formation, such as EMPGs and first galaxies, which fall into the low  $t_{\text{sf}}$  category, exhibit low He/H at low metallicity, as illustrated in Figs. 1(a, b). Therefore, including galaxies with low star formation efficiency in the analysis could lead to a steeper fitting line due to their high He/H ratios at low metallicities.

To investigate this quantitatively, it is essential to incorporate simulations that specifically include EMPGs and typical dwarf galaxies. These simulations must possess high mass resolution to accurately capture detailed

star formation histories and effectively simulate starburst phenomena. However, conducting such simulations remains a significant challenge for future research. In particular, such a simulation may answer the question of whether EMPGs are local analogs of the first galaxies. Additionally, it is anticipated that these simulations will extend to normal dwarf galaxies, providing an opportunity to validate the  $t_{\text{sf}}$  dependence of the He/H–O/H relationship, as derived from our one-zone model results.

Another future task is to expand the dataset of He/H and O/H observations in galaxies with low metallicity and compare the fitting curves across different specific SFRs. This requires deep spectroscopic observations of a lot of dwarf galaxies including EMPGs. Information on the He/H–O/H relation of high redshift galaxies, as observed by JWST, is also important and will be the subject of future work.

## 5. SUMMARY

We investigate the chemical evolution of EMPGs and first galaxies employing both the one-zone box model and cosmological hydrodynamic simulations with star formation and SN feedback models.

The findings from our one-zone model calculations indicate that galaxies with long star formation timescales achieve high He/H at low metallicity, similar to observations, when using the Limongi & Chieffi (2018) yield, which includes metal enrichment from the WR star. Similarly, this yield also reproduces Fe/O at low metallicity for long star formation timescales, comparable to the EMPGs observations. In contrast, the slope of the He/H–O/H relation is moderate when the star formation timescale is short or when chemical enrichment from the WR star is not considered. The yield from Nomoto et al. (2013), which considers PISN in Pop III, is expected to have high Fe/O at young ages, but does not reproduce the high Fe/O observed in EMPGs because it is immediately contaminated with oxygen by CCSNe.

We performed cosmological hydrodynamic simulations to calculate a more realistic baryon cycle in the first galaxies. Our simulated first galaxy successfully reproduces the stellar mass and SFR of GN-z11. However, it falls short in a few aspects: it did not match the high Fe/O ratios observed by JWST, tended to overproduce metal elements, and failed to produce any gas with high He/H with low O/H. The He/H–O/H relation for the interior of the first galaxies, spatially resolved at high resolution, also shows that the dispersion is smaller than observed. The fact that none of the gas particles in the galaxy have high He abundances at low metallicities, as seen in the observations, suggests that the high He/H

observed at low O/H levels is not simply the result of observing a particular component of gas in the galaxy.

Furthermore, a zoom-in simulation of the first galaxies with different CCSNe yields was also performed to discuss the effect of metal enrichment from rotating stars. We find that the He/H–O/H dispersion is larger in Limongi & Chieffi (2018) than in Nomoto et al. (2013), but not enough to reproduce the observed He/H dispersion. In both CCSN yields, the slope of the He/H–O/H relation is more gentle than observed. This is due to active star formation in the first galaxies, corresponding to the short  $t_{\text{sf}}$  in the one-zone model results. To determine the primordial He abundance from galaxy observations, it is desirable to use galaxies with similar star formation histories, and a sample of low-metallicity galaxies with high SFR is particularly suited for estimation because of their low He enrichment.

Finally, we discuss future prospects. To more accurately reproduce the observed chemical abundance in young, low-metallicity galaxies such as EMPGs and first galaxies, a sufficiently high-resolution cosmological hydrodynamic simulation capable of handling realistic baryon cycles down to  $z = 0$  needs to be performed. These future simulations should particularly focus on simulating EMPGs and typical dwarf galaxies, capturing the nuances of starburst phenomena and the impact of different yield models, such as those of rotating stars. Additionally, expanding the dataset of He/H and O/H

observations in low-metallicity galaxies will be crucial. This entails deep spectroscopic observations of a wide array of dwarf galaxies, including EMPGs. The emerging data from the JWST on high-redshift galaxies will also play a pivotal role in refining our understanding of the He/H–O/H relationship and its dependence on specific star formation rates. These steps will significantly contribute to confirming whether EMPGs are indeed local analogs of the first galaxies and provide a more comprehensive understanding of their chemical evolution.

## 6. ACKNOWLEDGMENTS

We are grateful to Volker Springel for providing the original version of GADGET-3, on which the GADGET3-OSAKA code is based. Numerical computations were carried out on the Cray XC50 at the Center for Computational Astrophysics, National Astronomical Observatory of Japan, and the OCTOPUS and SQUID at the Cybermedia Center, Osaka University, and the OAKFOREST-PACS as part of the HPCI system Research Project (hp200041, hp220044, hp230089). This work is supported in part by the MEXT/JSPS KAKENHI grant numbers 20H00180, 22K21349 (K.N.), 22KJ0157, 20K14532, 21H04499, 21K03614, 22H01259 (Y.H.), 21J20785 (Y.I.). This work was supported by JST SPRING, grant number JPMJSP2138 (K.F.). K.N. acknowledges the travel support from the Kavli IPMU, World Premier Research Center Initiative (WPI), where part of this work was conducted.

## APPENDIX

### A. ONE-ZONE BOX MODEL

In this section, we present the governing equations and parameters of our one-zone model for the chemical evolution of galaxies, which assumes that the cold ISM is uniformly enriched by metals. Treatment of the chemical enrichment of ISM in this approximation is well established (e.g. Tinsley 1980; Matteucci & Greggio 1986; Matteucci & Franco 1989; Prantzos et al. 1993; Timmes et al. 1995; Chiappini et al. 1997; Matteucci 2001; Kobayashi et al. 2006; Suzuki & Maeda 2018; Kobayashi et al. 2020; Kobayashi & Ferrara 2023). In this study, we mainly follow Kobayashi & Taylor (2023).

The time evolution of the mass fraction  $Z_i$  of the  $i$ th component (H, He, metals) in the gas phase of a one-zone box can be written as A1

$$\frac{d(Z_i(t)f_{\text{gas}}(t))}{dt} = Z_{i,\text{in}}(t)\dot{R}_{\text{in}}(t) + \dot{E}_{\text{ej},i}(t) - Z_i(t)\psi(t) - Z_i(t)\dot{R}_{\text{out}}(t), \quad (\text{A1})$$

where each term on the right-hand side corresponds to gas inflow rate, element ejection rate into ISM from SNe, gas mass incorporated by stars during star formation, and gas outflow rate from the galaxy by SNe. Here,  $f_{\text{gas}}$  is the total gas mass in the system of a unit mass,  $Z_{i,\text{in}}$  is the mass ratio of the  $i$ th component in the accreted gas,  $\dot{R}_{\text{in}}$  is the gas accretion rate,  $\psi$  is the star formation rate,  $\dot{R}_{\text{out}}$  is the mass outflow rate, and  $\dot{E}_{\text{ej},i}$  is the mass ejection rate into the ISM by the SNe. In this paper, the metallicity of the accreted gas is set to  $f_{\text{inf}} = Z_{i,\text{in}}/Z_i = 0, 0.01, 0.1$ .

The gas mass accretion rate is assumed as

$$\dot{R}_{\text{in}}(t) = \frac{1}{t_{\text{in}}} \exp\left(-\frac{t}{t_{\text{in}}}\right), \quad (\text{A2})$$

where  $t_{\text{in}}$  is the gas accretion timescale.

We assume the SFR as

$$\psi(t) = \frac{f_{\text{gas}}(t)}{t_{\text{sf}}}, \quad (\text{A3})$$

where  $t_{\text{sf}}$  is the time scale of star formation.

The outflow rate is usually taken as  $\dot{R}_{\text{out}} = f_{\text{o}}\psi$ . However, we use SN energy directly, and calculate the outflow rate as follows:

$$\dot{R}_{\text{out}}(t) = \dot{e}_{\text{SN}}(t) \frac{100}{10^{51}} \times f_{\text{o}}, \quad (\text{A4})$$

where the energy injection rate by SN,  $\dot{e}_{\text{SN}}(t)$ , is computed as

$$\dot{e}_{\text{SN}}(t) = \int_0^t \dot{E}_{\text{CCSN,SNIa}}(t - t_{\text{form}}) \psi(t_{\text{form}}) dt_{\text{form}}. \quad (\text{A5})$$

Here,  $\dot{E}_{\text{CCSN,SNIa}}(t - t_{\text{form}})$  is the energy emitted per unit time per unit mass by CCSNe and SN Ia from individual star clusters, which depends on the SN event rate and IMF. Therefore,  $\dot{E}_{\text{CCSN,SNIa}}$  is dependent on the current time  $t$  and the star cluster's formation time  $t_{\text{form}}$ . Since  $\dot{E}_{\text{CCSN,SNIa}}(t - t_{\text{form}})$  is the energy release per unit mass, we multiply by  $\psi$  to use the mass at the formation time.

Similarly to Equation A5, the element ejection rate due to SN can be written as

$$\dot{E}_{\text{ej},i}(t) = \int_0^t \psi(t_{\text{form}}) \dot{Y}_i(t - t_{\text{form}}) dt_{\text{form}}, \quad (\text{A6})$$

where  $\dot{Y}_i(t - t_{\text{form}})$  represents the mass ejection rate per unit mass of the star cluster per unit time for  $i$ th elements, originating from the stellar cluster. Quantities  $\dot{E}_{\text{CCSN,SNIa}}(t - t_{\text{form}})$  and  $\dot{Y}_i(t - t_{\text{form}})$  were calculated using CELIB (Saitoh 2016, 2017).

To enhance understanding of the one-zone model calculation, we provide a comparison of fundamental outcomes from different yield models. Figure 6 shows the evolutionary track of the one-zone model calculation presented in Fig. 1(c,d). The top four panels use the Nomoto et al. (2013) yield for the CCSN yield, and the bottom four panels use the Limongi & Chieffi (2018) yield. Each of the four panels shows the variation in parameters  $t_{\text{sf}}$ ,  $t_{\text{in}}$ ,  $f_{\text{in}}$ , and  $f_{\text{o}}$  clockwise. The following parameters were chosen as fiducial values:  $t_{\text{sf}} = 10^9$ ,  $t_{\text{in}} = 10^9$ ,  $f_{\text{in}} = 0.0$ , and  $f_{\text{o}} = 0.1$ . The pathway of chemical evolution is influenced by the choice of yields, with  $t_{\text{sf}}$  playing a primary role. A larger value of  $f_{\text{o}}$  leads to an increase in the Fe/O due to SN Ia contributions, accentuating the impact of gas outflow and the most recent metal enrichment. The evolutionary tracks in the upper four panels begin with a high Fe/O ratio, approximately 0.35, a consequence of metal enrichments by PISN from Pop III stars. In the Limongi & Chieffi (2018) yield, on the other hand, metal enrichment by CCSNe is mainly contributed by the WR star, resulting in low Fe/O values at low metallicities in the one-zone model.

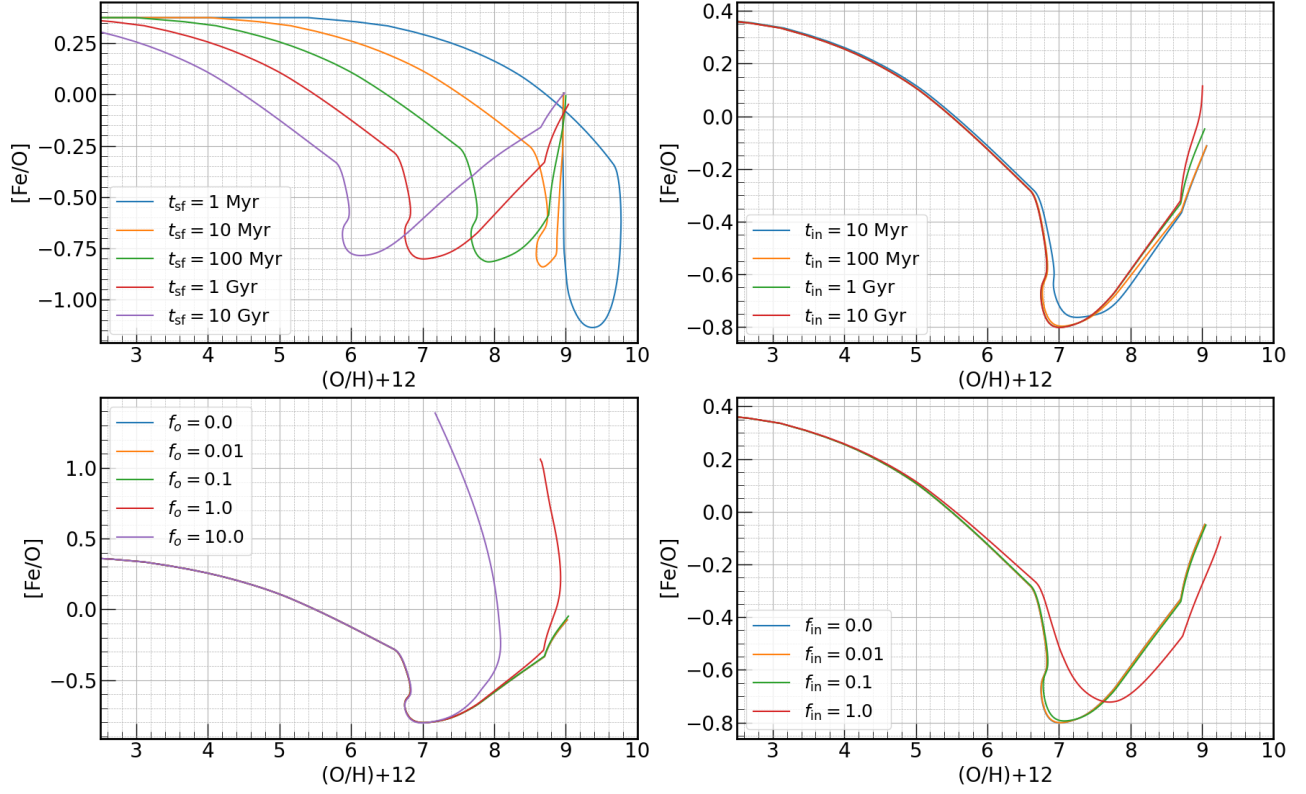
## B. CELIB RESULT of Fe/O

To help understand the results of different yield models, we present the time evolution of Fe/O emitted from a simple stellar population calculated using CELIB in Figure 7. The left panel shows the Nomoto et al. (2013) yield, and the right panel for the Limongi & Chieffi (2018) yield. Different line color indicates the metallicity of the population. At  $t = 10^{7.6}$  yr, Fe release by SNIa begins to occur, increasing Fe/O in both panels. A much higher Fe/O at  $10^{6.5}$  yr for  $Z = 10^{-7}$  (Pop III) case in the left panel is due to metal enrichment by PISN.

## REFERENCES

- |   |  |
|---|--|
| <p>Agertz, O., Pontzen, A., Read, J. I., et al. 2020, MNRAS, 491, 1656, doi: <a href="https://doi.org/10.1093/mnras/stz3053">10.1093/mnras/stz3053</a></p> <p>Arrabal Haro, P., Dickinson, M., Finkelstein, S. L., et al. 2023a, ApJL, 951, L22, doi: <a href="https://doi.org/10.3847/2041-8213/acdd54">10.3847/2041-8213/acdd54</a></p> <p>—. 2023b, Nature, 622, 707, doi: <a href="https://doi.org/10.1038/s41586-023-06521-7">10.1038/s41586-023-06521-7</a></p> | <p>Barkat, Z., Rakavy, G., &amp; Sack, N. 1967, PhRvL, 18, 379, doi: <a href="https://doi.org/10.1103/PhysRevLett.18.379">10.1103/PhysRevLett.18.379</a></p> <p>Benitez-Llambay, A., &amp; Frenk, C. 2020, MNRAS, 498, 4887, doi: <a href="https://doi.org/10.1093/mnras/staa2698">10.1093/mnras/staa2698</a></p> <p>Bunker, A. J., Saxena, A., Cameron, A. J., et al. 2023, A&amp;A, 677, A88, doi: <a href="https://doi.org/10.1051/0004-6361/202346159">10.1051/0004-6361/202346159</a></p> |
|---|--|

## Nomoto et al. 2013



## Limongi &amp; Chieffi 2018

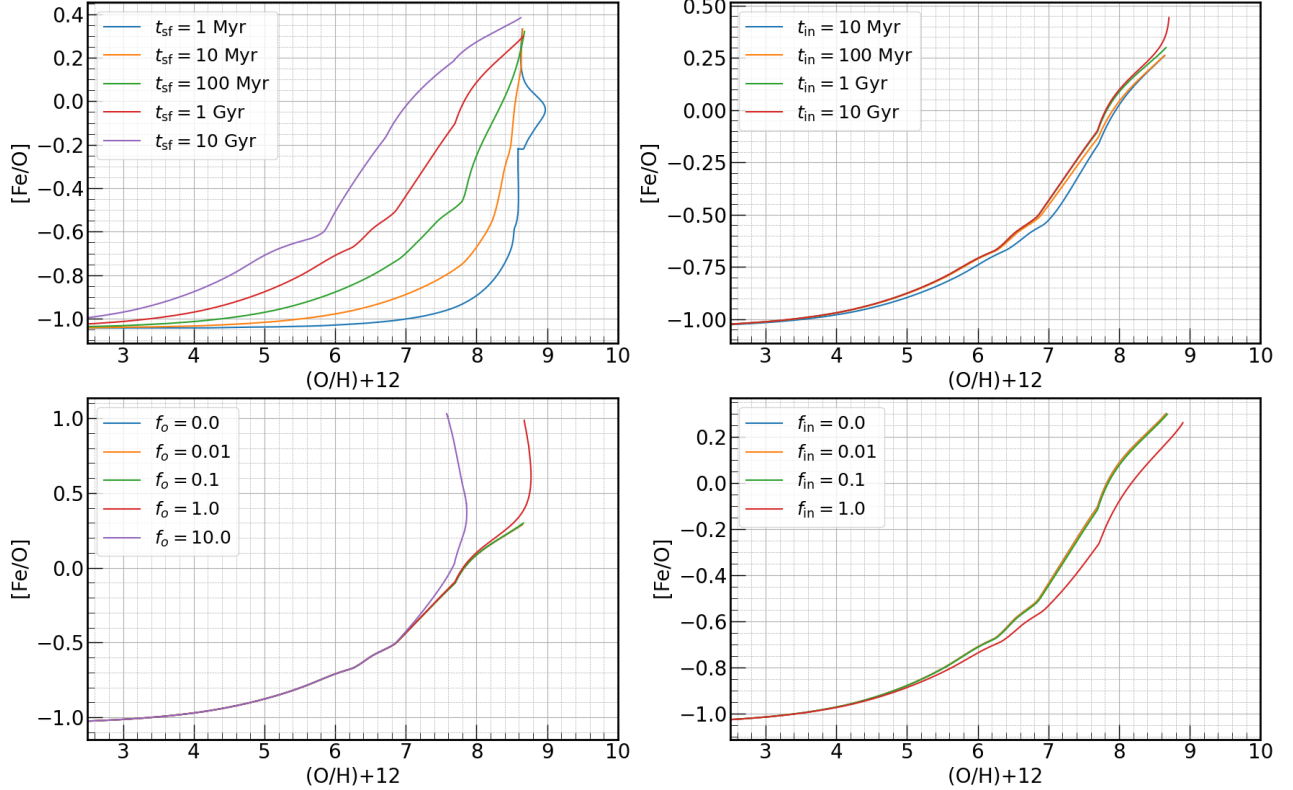


**Figure 6.** Chemical evolution track of  $\text{Fe}/\text{O}$  vs.  $\text{O}/\text{H}$  from our one-zone model. The top 4 figures are the results of the Nomoto et al. (2013) yield, and the bottom 4 figures are the results of the Limongi & Chieffi (2018) yield.

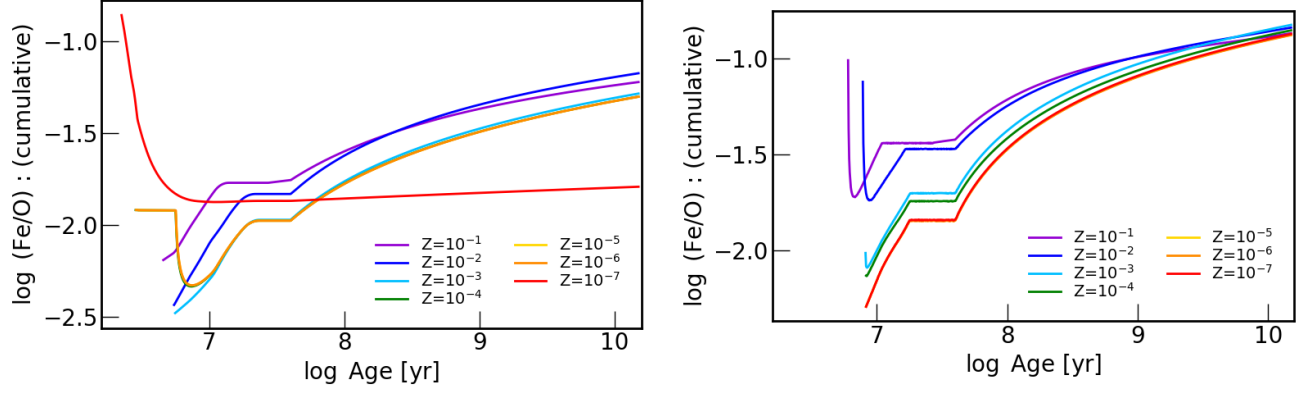


**Figure 7.** Evolution of the ejecta's chemical abundance of Fe/O from CELIB for a simple stellar population. The left panel is for the [Nomoto et al. \(2013\)](#) yield, and the right panel is for the [Limongi & Chieffi \(2018\)](#) yield.

- Cameron, A. J., Katz, H., Rey, M. P., & Saxena, A. 2023, *MNRAS*, 523, 3516, doi: [10.1093/mnras/stad1579](#)
- Campbell, S. W., & Lattanzio, J. C. 2008, *A&A*, 490, 769, doi: [10.1051/0004-6361:200809597](#)
- Chabrier, G. 2003, *PASP*, 115, 763, doi: [10.1086/376392](#)
- Chiappini, C., Matteucci, F., & Gratton, R. 1997, *ApJ*, 477, 765, doi: [10.1086/303726](#)
- Curti, M., D'Eugenio, F., Carniani, S., et al. 2023a, *MNRAS*, 518, 425, doi: [10.1093/mnras/stac2737](#)
- Curti, M., Maiolino, R., Curtis-Lake, E., et al. 2023b, *arXiv e-prints*, arXiv:2304.08516, doi: [10.48550/arXiv.2304.08516](#)
- Curtis-Lake, E., Carniani, S., Cameron, A., et al. 2023, *Nature Astronomy*, 7, 622, doi: [10.1038/s41550-023-01918-w](#)
- Doherty, C. L., Gil-Pons, P., Lau, H. H. B., Lattanzio, J. C., & Siess, L. 2014, *MNRAS*, 437, 195, doi: [10.1093/mnras/stt1877](#)
- Fukushima, K., Nagamine, K., & Shimizu, I. 2023, *MNRAS*, 525, 3760, doi: [10.1093/mnras/stad2526](#)
- Gil-Pons, P., Doherty, C. L., Lau, H., et al. 2013, *A&A*, 557, A106, doi: [10.1051/0004-6361/201321127](#)
- Gutcke, T. A., Pakmor, R., Naab, T., & Springel, V. 2022, *MNRAS*, 513, 1372, doi: [10.1093/mnras/stac867](#)
- Haardt, F., & Madau, P. 2012, *ApJ*, 746, 125, doi: [10.1088/0004-637X/746/2/125](#)
- Hahn, O., & Abel, T. 2011, *MNRAS*, 415, 2101, doi: [10.1111/j.1365-2966.2011.18820.x](#)
- Harikane, Y., Nakajima, K., Ouchi, M., et al. 2024, *ApJ*, 960, 56, doi: [10.3847/1538-4357/ad0b7e](#)
- Harikane, Y., Ouchi, M., Oguri, M., et al. 2023, *ApJS*, 265, 5, doi: [10.3847/1538-4365/acaaa9](#)
- Heger, A., & Woosley, S. E. 2002, *ApJ*, 567, 532, doi: [10.1086/338487](#)
- Hirai, Y., Ishimaru, Y., Saitoh, T. R., et al. 2017, *MNRAS*, 466, 2474, doi: [10.1093/mnras/stw3342](#)
- Hopkins, P. F. 2015, *MNRAS*, 450, 53, doi: [10.1093/mnras/stv195](#)
- Hopkins, P. F., Wetzel, A., Kereš, D., et al. 2018, *MNRAS*, 480, 800, doi: [10.1093/mnras/sty1690](#)
- Hsyu, T., Cooke, R. J., Prochaska, J. X., & Bolte, M. 2020, *ApJ*, 896, 77, doi: [10.3847/1538-4357/ab91af](#)
- Isobe, Y., Ouchi, M., Suzuki, A., et al. 2022, *ApJ*, 925, 111, doi: [10.3847/1538-4357/ac3509](#)
- Isobe, Y., Ouchi, M., Tominaga, N., et al. 2023, *ApJ*, 959, 100, doi: [10.3847/1538-4357/ad09be](#)
- Izotov, Y. I., Thuan, T. X., Guseva, N. G., & Liss, S. E. 2018a, *MNRAS*, 473, 1956, doi: [10.1093/mnras/stx2478](#)
- Izotov, Y. I., Worseck, G., Schaerer, D., et al. 2018b, *MNRAS*, 478, 4851, doi: [10.1093/mnras/sty1378](#)
- Johnson, J. L., Dalla Vecchia, C., & Khochfar, S. 2013, *MNRAS*, 428, 1857, doi: [10.1093/mnras/sts011](#)
- Karakas, A. I. 2010, *MNRAS*, 403, 1413, doi: [10.1111/j.1365-2966.2009.16198.x](#)
- Kimm, T., & Cen, R. 2014, *ApJ*, 788, 121, doi: [10.1088/0004-637X/788/2/121](#)
- Kobayashi, C., & Ferrara, A. 2023, *arXiv e-prints*, arXiv:2308.15583, doi: [10.48550/arXiv.2308.15583](#)
- Kobayashi, C., Karakas, A. I., & Lugaro, M. 2020, *ApJ*, 900, 179, doi: [10.3847/1538-4357/abae65](#)
- Kobayashi, C., & Taylor, P. 2023, *arXiv e-prints*, arXiv:2302.07255, doi: [10.48550/arXiv.2302.07255](#)
- Kobayashi, C., Umeda, H., Nomoto, K., Tominaga, N., & Ohkubo, T. 2006, *ApJ*, 653, 1145, doi: [10.1086/508914](#)
- Kojima, T., Ouchi, M., Rauch, M., et al. 2020, *ApJ*, 898, 142, doi: [10.3847/1538-4357/aba047](#)
- . 2021, *ApJ*, 913, 22, doi: [10.3847/1538-4357/abec3d](#)
- Limongi, M., & Chieffi, A. 2018, *ApJS*, 237, 13, doi: [10.3847/1538-4365/aac24](#)

- Maoz, D., & Mannucci, F. 2012, *PASA*, 29, 447, doi: [10.1071/AS11052](https://doi.org/10.1071/AS11052)
- Maoz, D., Mannucci, F., & Nelemans, G. 2014, *ARA&A*, 52, 107, doi: [10.1146/annurev-astro-082812-141031](https://doi.org/10.1146/annurev-astro-082812-141031)
- Matsumoto, A., Ouchi, M., Nakajima, K., et al. 2022, *ApJ*, 941, 167, doi: [10.3847/1538-4357/ac9ea1](https://doi.org/10.3847/1538-4357/ac9ea1)
- Matteucci, F. 2001, *The chemical evolution of the Galaxy*, Vol. 253, doi: [10.1007/978-94-010-0967-6](https://doi.org/10.1007/978-94-010-0967-6)
- Matteucci, F., & Francois, P. 1989, *MNRAS*, 239, 885, doi: [10.1093/mnras/239.3.885](https://doi.org/10.1093/mnras/239.3.885)
- Matteucci, F., & Greggio, L. 1986, *A&A*, 154, 279
- Nagamine, K., Shimizu, I., Fujita, K., et al. 2021, *ApJ*, 914, 66, doi: [10.3847/1538-4357/abfa16](https://doi.org/10.3847/1538-4357/abfa16)
- Nakajima, K., Ouchi, M., Isobe, Y., et al. 2023, arXiv e-prints, arXiv:2301.12825, doi: [10.48550/arXiv.2301.12825](https://doi.org/10.48550/arXiv.2301.12825)
- Nomoto, K., Kobayashi, C., & Tominaga, N. 2013, *ARA&A*, 51, 457, doi: [10.1146/annurev-astro-082812-140956](https://doi.org/10.1146/annurev-astro-082812-140956)
- Planck Collaboration, Ade, P. A. R., Aghanim, N., et al. 2016, *A&A*, 594, A13, doi: [10.1051/0004-6361/201525830](https://doi.org/10.1051/0004-6361/201525830)
- Prantzos, N., Casse, M., & Vangioni-Flam, E. 1993, *ApJ*, 403, 630, doi: [10.1086/172233](https://doi.org/10.1086/172233)
- Revaz, Y., & Jablonka, P. 2018, *A&A*, 616, A96, doi: [10.1051/0004-6361/201832669](https://doi.org/10.1051/0004-6361/201832669)
- Roberts-Borsani, G., Treu, T., Chen, W., et al. 2023, *Nature*, 618, 480, doi: [10.1038/s41586-023-05994-w](https://doi.org/10.1038/s41586-023-05994-w)
- Rodriguez Wimberly, M. K., Cooper, M. C., Fillingham, S. P., et al. 2019, *MNRAS*, 483, 4031, doi: [10.1093/mnras/sty3357](https://doi.org/10.1093/mnras/sty3357)
- Romano-Díaz, E., Shlosman, I., Choi, J.-H., & Sadoun, R. 2014, *ApJL*, 790, L32, doi: [10.1088/2041-8205/790/2/L32](https://doi.org/10.1088/2041-8205/790/2/L32)
- Saitoh, T. R. 2016, *CELib: Software library for simulations of chemical evolution*. <http://ascl.net/1612.016>
- . 2017, *AJ*, 153, 85, doi: [10.3847/1538-3881/153/2/85](https://doi.org/10.3847/1538-3881/153/2/85)
- Seitenzahl, I. R., Ciaraldi-Schoolmann, F., Röpke, F. K., et al. 2013, *MNRAS*, 429, 1156, doi: [10.1093/mnras/sts402](https://doi.org/10.1093/mnras/sts402)
- Senchyna, P., Plat, A., Stark, D. P., & Rudie, G. C. 2023, arXiv e-prints, arXiv:2303.04179, doi: [10.48550/arXiv.2303.04179](https://doi.org/10.48550/arXiv.2303.04179)
- Shimizu, I., Todoroki, K., Yajima, H., & Nagamine, K. 2019, *MNRAS*, 484, 2632, doi: [10.1093/mnras/stz098](https://doi.org/10.1093/mnras/stz098)
- Smith, B. D., Bryan, G. L., Glover, S. C. O., et al. 2017, *MNRAS*, 466, 2217, doi: [10.1093/mnras/stw3291](https://doi.org/10.1093/mnras/stw3291)
- Springel, V. 2005, *MNRAS*, 364, 1105, doi: [10.1111/j.1365-2966.2005.09655.x](https://doi.org/10.1111/j.1365-2966.2005.09655.x)
- Susa, H., Hasegawa, K., & Tominaga, N. 2014, *ApJ*, 792, 32, doi: [10.1088/0004-637X/792/1/32](https://doi.org/10.1088/0004-637X/792/1/32)
- Suzuki, A., & Maeda, K. 2018, *ApJ*, 852, 101, doi: [10.3847/1538-4357/aaa024](https://doi.org/10.3847/1538-4357/aaa024)
- Timmes, F. X., Woosley, S. E., & Weaver, T. A. 1995, *ApJS*, 98, 617, doi: [10.1086/192172](https://doi.org/10.1086/192172)
- Tinsley, B. M. 1980, *FCPh*, 5, 287
- Totani, T., Morokuma, T., Oda, T., Doi, M., & Yasuda, N. 2008, *PASJ*, 60, 1327, doi: [10.1093/pasj/60.6.1327](https://doi.org/10.1093/pasj/60.6.1327)
- Umeda, H., & Nomoto, K. 2002, *ApJ*, 565, 385, doi: [10.1086/323946](https://doi.org/10.1086/323946)
- Vanzella, E., Loiacono, F., Bergamini, P., et al. 2023, *A&A*, 678, A173, doi: [10.1051/0004-6361/202346981](https://doi.org/10.1051/0004-6361/202346981)
- Ventura, P., Di Criscienzo, M., Carini, R., & D’Antona, F. 2013, *MNRAS*, 431, 3642, doi: [10.1093/mnras/stt444](https://doi.org/10.1093/mnras/stt444)
- Vincenzo, F., Kobayashi, C., & Taylor, P. 2018, *MNRAS*, 480, L38, doi: [10.1093/mnras/sly128](https://doi.org/10.1093/mnras/sly128)
- Vincenzo, F., Miglio, A., Kobayashi, C., Mackereth, J. T., & Montalbán, J. 2019, *A&A*, 630, A125, doi: [10.1051/0004-6361/201935886](https://doi.org/10.1051/0004-6361/201935886)
- Watanabe, K., Ouchi, M., Nakajima, K., et al. 2023, arXiv e-prints, arXiv:2305.02078, doi: [10.48550/arXiv.2305.02078](https://doi.org/10.48550/arXiv.2305.02078)
- Wetzel, A. R., Hopkins, P. F., Kim, J.-h., et al. 2016, *ApJL*, 827, L23, doi: [10.3847/2041-8205/827/2/L23](https://doi.org/10.3847/2041-8205/827/2/L23)
- Wheeler, C., Hopkins, P. F., Pace, A. B., et al. 2019, *MNRAS*, 490, 4447, doi: [10.1093/mnras/stz2887](https://doi.org/10.1093/mnras/stz2887)
- Williams, H., Kelly, P. L., Chen, W., et al. 2023, *Science*, 380, 416, doi: [10.1126/science.adf5307](https://doi.org/10.1126/science.adf5307)
- Wise, J. H., Turk, M. J., Norman, M. L., & Abel, T. 2012, *ApJ*, 745, 50, doi: [10.1088/0004-637X/745/1/50](https://doi.org/10.1088/0004-637X/745/1/50)
- Yajima, H., Abe, M., Fukushima, H., et al. 2023, *MNRAS*, 525, 4832, doi: [10.1093/mnras/stad2497](https://doi.org/10.1093/mnras/stad2497)
- Yajima, H., Nagamine, K., Zhu, Q., Khochfar, S., & Dalla Vecchia, C. 2017, *ApJ*, 846, 30, doi: [10.3847/1538-4357/aa82b5](https://doi.org/10.3847/1538-4357/aa82b5)
- Yang, H., Malhotra, S., Rhoads, J. E., & Wang, J. 2017, *ApJ*, 847, 38, doi: [10.3847/1538-4357/aa8809](https://doi.org/10.3847/1538-4357/aa8809)